the effects of an oblique impact, this may explain the marked difference between the development of rings in the eastern and western sectors of the basin.

In addition to forming rings in approximately the correct locations (Fig. 1 and fig. S8B), models with pre-impact crustal thicknesses that range from 48 to 52 km also reproduce the azimuthally averaged crustal thickness profile derived from GRAIL gravity and LOLA topography (Fig. 3). Our modeling shows that ring location and fault offsets are highly dependent on impactor size and the pre-impact thermal gradient (figs. S9 and S10). In our best-fitting model, the region where crust is thinned from the pre-impact value extends to $R_{thin} \approx 200$ km. The parameter R_{thin} also provides an estimate for the radius of the zone of ejecta provenance or excavation cavity (*36*). In our best-fitting model of Orientale, these two metrics agree to within 5%. We favor the model with pre-impact crustal thickness of 52 km because it produces a thicker cap of cool crustal material at the center of the basin (Fig. 3), consistent with gravity observations.

Inverse models of GRAIL gravity data suggest that the Outer Rook and Cordillera are associated with localized crustal thinning and offsets at the crust-mantle interface (*2*). The crustal structure also reveals offsets at the crust-mantle interface that do not correlate with rings and may indicate additional subsurface faults. The faults with small offsets forming on either side of the Cordillera in our simulations may be consistent with these additional faults (Fig. 2). The amount of crustal thinning and magnitude of crust-mantle relief, however, depend on the assumptions of these inverse models (*2*). Our models exhibit local minima in the crustal thickness (Fig. 3) and offsets at the crust-mantle interface (Fig. 2) associated with the Outer Rook and Cordillera. These results are consistent with normal faults with offsets of a few kilometers cutting through the crust-mantle interface. The simple geometry of a normal fault with a dip angle of 50° and offset of 4 km cutting through 50-km-thick crust will create a ~40-km-wide region where the crust is thinned by ~3 km. This idealized fault geometry is similar to the modeled Outer Rook ring (Fig. 3, red curve 300 to 340 km from basin center). When extension occurs close to a fault (within ~40 km), the zone of crustal thinning is broader (Figs. 2 and 3 and fig. S8B). Inverse models of the crust-mantle interface are limited in resolution to a wavelength approximately equal to the crustal thickness. Thus, the predicted broader zone of extension may explain in part why the signature of the Cordillera is more robust than that of the Outer Rook (*2*). Similar local minima in crustal thickness as observed by GRAIL may reveal ring faults in highly degraded or mare-filled basins.

REFERENCES AND NOTES

1. J. W. Head, *Moon* **11**, 327–356 (1974).
2. M. T. Zuber *et al.*, *Science* **354**, 438–441 (2016).
3. A. L. Nahm, T. Öhman, D. A. Kring, *J. Geophys. Res. Planets* **118**, 190–205 (2013).
4. Y. N. Kattoum, J. C. Andrews-Hanna, *Icarus* **226**, 694–707 (2013).
5. D. M. H. Baker *et al.*, *Icarus* **214**, 377–393 (2011).
6. A. A. Amsden, H. M. Ruppel, C. W. Hirt, *SALE: A Simplified ALE Computer Program for Fluid Flow at Speeds* (Los Alamos National Laboratories Report LA-8095, 1980).
7. G. S. Collins, H. J. Melosh, B. A. Ivanov, *Meteorit. Planet. Sci.* **39**, 217–231 (2004).
8. K. Wünnemann, G. S. Collins, H. J. Melosh, *Icarus* **180**, 514–527 (2006).
9. R. W. K. Potter, D. A. Kring, G. S. Collins, W. S. Kiefer, P. J. McGovern, *J. Geophys. Res. Planets* **118**, 963–979 (2013).
10. R. W. K. Potter, *Icarus* **261**, 91–99 (2015).
11. A. M. Freed *et al.*, *J. Geophys. Res. Planets* **119**, 2378–2397 (2014).
12. K. Miljković *et al.*, *Science* **342**, 724–726 (2013).
13. M.-H. Zhu, K. Wünnemann, R. W. K. Potter, *J. Geophys. Res. Planets* **120**, 2118–2134 (2015).
14. G. S. Collins, *J. Geophys. Res. Planets* **119**, 2600–2619 (2014).
15. L. G. J. Montési, *J. Geophys. Res.* **107** (B3), 2045 (2002).
16. B. A. Ivanov, H. J. Melosh, E. Pierazzo, *Geol. Soc. Spec. Pap.*, 29–49 (2010).
17. See supplementary materials on *Science* Online.
18. M. Le Feuvre, M. A. Wieczorek, *Icarus* **214**, 1–20 (2011).
19. D. E. Smith *et al.*, *Icarus* 10.1016/j.icarus.2016.06.006 (2016).
20. M. A. Wieczorek *et al.*, *Science* **339**, 671–675 (2013).
21. R. W. K. Potter, D. A. Kring, G. S. Collins, W. S. Kiefer, P. J. McGovern, *Geophys. Res. Lett.* **39**, L18203 (2012).
22. M. Laneuville, M. A. Wieczorek, D. Breuer, N. Tosi, *J. Geophys. Res. Planets* **118**, 1435–1452 (2013).
23. R. B. Baldwin, *Phys. Earth Planet. Inter.* **6**, 327–339 (1972).
24. H. J. Melosh, W. B. McKinnon, *Geophys. Res. Lett.* **5**, 985–988 (1978).
25. J. W. Head, *Geophys. Res. Lett.* **37**, L02203 (2010).
26. C. A. Hodges, D. E. Wilhelms, *Icarus* **34**, 294–323 (1978).
27. G. S. Collins, H. J. Melosh, J. V. Morgan, M. R. Warner, *Icarus* **157**, 24–33 (2002).
28. L. C. Cheek, K. L. Donaldson Hanna, C. M. Pieters, J. W. Head, J. L. Whitten, *J. Geophys. Res. Planets* **118**, 1805–1820 (2013).
29. G. J. Taylor, M. A. Wieczorek, *Philos. Trans. R. Soc. A* **372**, 20130242 (2014).
30. P. D. Spudis, D. J. P. Martin, G. Kramer, *J. Geophys. Res. Planets* **119**, 19–29 (2014).
31. H. J. Melosh *et al.*, *Science* **340**, 1552–1555 (2013).
32. M. T. Zuber *et al.*, *Science* **339**, 668–671 (2013).
33. P. K. Byrne *et al.*, *Earth Planet. Sci. Lett.* **427**, 183–190 (2015).
34. W. M. Vaughan, J. W. Head, L. Wilson, P. C. Hess, *Icarus* **223**, 749–765 (2013).
35. S. R. Bratt, S. C. Solomon, J. W. Head, *J. Geophys. Res.* **90**, 12415–12433 (1985).
36. M. A. Wieczorek, R. J. Phillips, *Icarus* **139**, 246–259 (1999).

ACKNOWLEDGMENTS

We thank two anonymous reviewers for their thoughtful reviews; the developers of iSALE (www.isale-code.de/redmine/projects/iSALE), including K. Wünnemann, D. Elbeshausen, and B. Ivanov; and all those involved with the development and operations of the GRAIL spacecraft and the collection and reduction of the GRAIL data. This work was funded by the GRAIL mission, which is supported by the NASA Discovery Program and is performed under contract to the Massachusetts Institute of Technology and the Jet Propulsion Laboratory, California Institute of Technology. G.S.C. was funded by UK Science and Technology Facilities Council grant ST/N000803/1. At present, iSALE is not publicly available. It is distributed on a case-by-case basis to academic users in the impact community, strictly for noncommercial use. Scientists interested in using or developing iSALE should see www.isale-code.de/redmine/projects/isale/wiki/Terms_of_use for a description of application requirements. Model output has been published at the Harvard Dataverse, doi:10.7910/DVN/BH9UXW.

SUPPLEMENTARY MATERIALS

www.sciencemag.org/content/354/6311/441/suppl/DC1
Materials and Methods
Figs. S1 to S10
Tables S1 and S2
Movie S1
References (*37*–*55*)

5 May 2016; accepted 8 September 2016
10.1126/science.aag0518

CHEMICAL KINETICS

Direct frequency comb measurement of OD + CO → DOCO kinetics

B. J. Bjork,[1]* T. Q. Bui,[1] O. H. Heckl,[1] P. B. Changala,[1] B. Spaun,[1] P. Heu,[2] D. Follman,[2] C. Deutsch,[3] G. D. Cole,[2,3] M. Aspelmeyer,[4] M. Okumura,[5] J. Ye[1]*

The kinetics of the hydroxyl radical (OH) + carbon monoxide (CO) reaction, which is fundamental to both atmospheric and combustion chemistry, are complex because of the formation of the hydrocarboxyl radical (HOCO) intermediate. Despite extensive studies of this reaction, HOCO has not been observed under thermal reaction conditions. Exploiting the sensitive, broadband, and high-resolution capabilities of time-resolved cavity-enhanced direct frequency comb spectroscopy, we observed deuteroxyl radical (OD) + CO reaction kinetics and detected stabilized *trans*-DOCO, the deuterated analog of *trans*-HOCO. By simultaneously measuring the time-dependent concentrations of the *trans*-DOCO and OD species, we observed unambiguous low-pressure termolecular dependence of the reaction rate coefficients for N_2 and CO bath gases. These results confirm the HOCO formation mechanism and quantify its yield.

The apparent simplicity of the gas-phase bimolecular reaction kinetics of free radicals often belies the complexity of the underlying dynamics. Reactions occur on multidimensional potential energy surfaces that can host multiple prereactive and bound intermediate complexes, as well as multiple transition states. As a result, effective bimolecular rate coefficients often exhibit complex temperature and pressure dependences. The importance of free radical reactions in processes such as combustion and air pollution chemistry has motivated efforts to determine these rate constants both experimentally and theoretically. Quantitative ab initio modeling of kinetics remains a major contemporary challenge (*1*), requiring accurate quantum chemical calculations of energies, frequencies, and anharmonicities; master equation

Downloaded from http://science.sciencemag.org/ on October 27, 2016

modeling; calculation of energy transfer dynamics; and, when necessary, calculation of tunneling and nonstatistical behavior. Experimental detection of the transient intermediates, which is the key to unraveling the dynamics, is frequently challenging.

The reaction of hydroxyl radical with CO

$$OH + CO \rightarrow H + CO_2,\ \Delta_r E_0 = -103.29\ kJ\ mol^{-1} \quad (1)$$

($\Delta_r E_0$, standard energy of the reaction at 0 K) has been extensively studied over the past four decades because of its central role in atmospheric and combustion chemistry (*2*); it has come to serve as a benchmark for state-of-the-art studies of the chemical kinetics of complex bimolecular reactions (*3*, *4*). In Earth's atmosphere, OH is critical as the primary daytime oxidant (*5*, *6*). CO, a byproduct of fossil fuel burning and hydrocarbon oxidation, acts through the reaction in Eq. 1 as an important global sink for OH radicals; this reaction is the dominant OH loss process in the free troposphere. In fossil fuel combustion, OH + CO is the final step that oxidizes CO to CO_2 and is responsible for a large amount of the heat released.

The rate of the reaction in Eq. 1 is pressure-dependent and exhibits an anomalous temperature dependence, which led Smith and Zellner (*7*) to propose that the reaction proceeds through a highly energized, strongly bound intermediate, HOCO, the hydrocarboxyl radical (Fig. 1A, inset). Formation of H + CO_2 products is an example of a chemically activated reaction. The course of the reaction is governed by the dynamics on the potential energy surface, shown schematically in Fig. 1A. The OH and CO pass through a prereactive weakly bound OH–CO complex to form a highly energized HOCO* (where the asterisk denotes vibrational excitation) in one of two isomers, *trans*-HOCO or the less stable *cis*-HOCO (*2*). In the low-pressure limit at room temperature, HOCO* primarily back-reacts to OH + CO, but there is a small probability of overcoming the low barrier (8.16 kJ mol^{-1}) and reacting to form H + CO_2. In the presence of buffer gas, energy transfer by collisions with third bodies M (termolecular process) can deactivate or further activate the HOCO*. Deactivation can lead to the formation of stable, thermalized HOCO products (reaction 1a in Fig. 1A, inset), which diminishes the formation of H + CO_2 (reaction 1b in Fig. 1A, inset). Approaching the high-pressure limit, HOCO formation becomes the dominant channel, and H + CO_2 product formation decreases. The overall reaction rate is characterized by an effective bimolecular rate constant $k_1([M],T) = k_{1a}([M],T) + k_{1b}([M],T)$, where T is temperature (*8*–*12*).

There have been numerous experimental studies of the temperature and pressure dependence of the overall rate coefficient $k_1([M],T)$; these all have measured OH loss in the presence of CO (*9*, *11*–*17*). In principle, master equation calculations with accurate potential energy surfaces within a statistical rate theory can compute $k_1([M],T)$, but a priori kinetics are rarely possible because the energy transfer dynamics are generally not known. A number of studies have thus fit the theoretical models to the observed overall rate constants, using a small number of parameters to describe collisional energy relaxation and activation (*9*, *11*, *15*, *16*, *18*, *19*). Although these previous studies have had success in describing $k_1([M],T)$, they do not capture the dynamics that would be revealed from the pressure-dependent branching between stabilization of HOCO and barrier crossing to form H + CO_2 products. Detection of the stabilized HOCO intermediate and measurement of its pressure-dependent yield would confirm the reaction mechanism and quantitatively test theoretical models. The spectroscopy of HOCO is well established, and recently HOCO has been observed in the OH + CO reaction generated in a discharge (*20*–*22*); however, measurements under thermal conditions are necessary to derive rate constants.

To directly and simultaneously measure the time-dependent concentrations of reactive radical intermediates such as HOCO and OH, we applied the recently developed technique of time-resolved direct frequency comb spectroscopy (TRFCS) (*23*). The massively parallel nature of frequency comb spectroscopy allows time-resolved, simultaneous detection of a number of key species, including intermediates and primary products, with high spectral and temporal resolution. The light source is a mid–infrared (IR) (wavelength $\lambda \approx 3$ to 5 μm) frequency comb, generated from an optical parametric oscillator (OPO) synchronously pumped with a high-repetition-rate (f_{rep} = 136 MHz) mode-locked femtosecond fiber laser (*24*). The OPO spectrum is composed of spectrally narrow comb teeth evenly spaced by f_{rep} and shifted by an offset frequency, f_0. By matching and locking the free spectral range of the enhancement cavity to $2 \times f_{rep}$, we keep the full comb spectrum resonant with the cavity during the data acquisition. The broadband transmitted light (~65 cm^{-1} bandwidth, ~7100 comb teeth) is spatially dispersed in two dimensions by a virtually imaged phased array etalon and a grating combination and is then imaged onto an InSb camera (fig. S1). Absorption spectra are constructed from these images as a function of time (with a resolution of ≥10 μs determined by the camera integration time), which are compared with known molecular line intensities to obtain absolute concentrations. The absorption detection sensitivity is greatly enhanced with our high-finesse ($F \approx 4100$) optical cavity that employs mid-IR mirrors with low-loss crystalline coatings. These mirrors, with a center wavelength of 3.72 μm and a spectral bandwidth of about 100 nm, have substantially lower optical losses and hence yield enhanced cavity contrast compared with traditional amorphous coatings [as covered in detail in (*25*)], enabling an improved sensitivity by a factor of 10 for the direct detection of *trans*-DOCO.

In this experiment, we studied the deuterium analog of Eq. 1, OD + CO → D + CO_2, exploiting the sensitivity and resolution of TRFCS to detect the reactant OD (in vibrational level, v = 0

[1]JILA, National Institute of Standards and Technology and University of Colorado, and Department of Physics, University of Colorado, Boulder, CO 80309, USA. [2]Crystalline Mirror Solutions, 114 East Haley Street, Suite G, Santa Barbara, CA 93101, USA. [3]Crystalline Mirror Solutions, Parkring 10, 1010 Vienna, Austria. [4]Vienna Center for Quantum Science and Technology, Faculty of Physics, University of Vienna, 1090 Vienna, Austria. [5]Arthur Amos Noyes Laboratory of Chemical Physics, Division of Chemistry and Chemical Engineering, California Institute of Technology, 1200 East California Boulevard, Pasadena, CA 91125, USA.
***Corresponding author. Email: bryce.bjork@colorado.edu (B.J.B.); ye@jila.colorado.edu (J.Y.)**

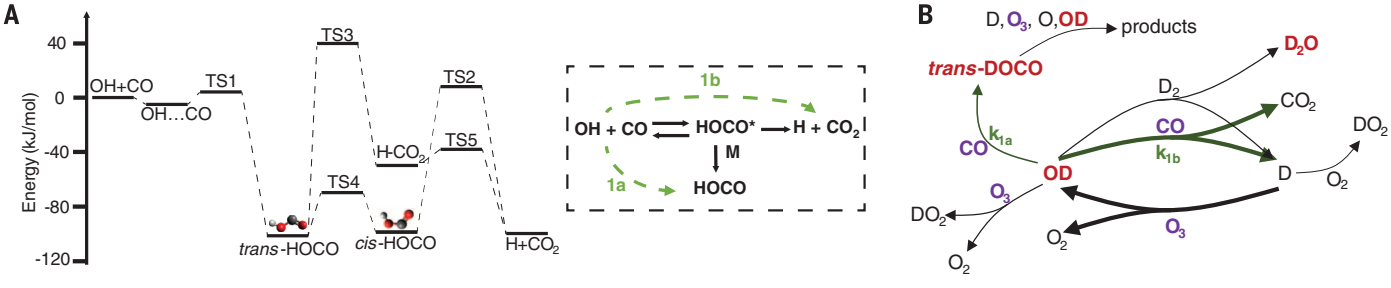

Fig. 1. Energetics of the OH + CO → H + CO_2 reaction. (**A**) Potential energy surface, with energies taken from Nguyen *et al*. (*2*). OH + CO → H + CO_2 proceeds through vibrationally excited HOCO*, which is either deactivated by bath gas M or reacts to form H + CO_2. The inset shows the simplified OH + CO reaction mechanism. TS, transition state. (**B**) Schematic showing the most important reactions in our system. Time-dependent concentrations of *trans*-DOCO, OD(v = 0), OD(v = 1), and D_2O (red) are measured by cavity-enhanced absorption spectroscopy; the concentrations of the precursors (purple) are set by flow controllers or meters. O_3 is measured by UV absorption.

Downloaded from http://science.sciencemag.org/ on October 27, 2016

and v = 1 states) and the product *trans*-DOCO by absorption spectroscopy in a pulsed-laser-photolysis flow cell experiment. We sought to measure the pressure-dependent effective bimolecular rate coefficients and the yield of *trans*-DOCO at total pressures of 27 to 75 torr (3.3 to 10 kPa). Such measurements would be especially sensitive to the competition between termolecular DOCO stabilization and the reaction to form D + CO_2. Detection of the deuterated species allowed us to avoid atmospheric water interference in our spectra. We further anticipated that the yield of stable DOCO would be higher, because deuteration substantially reduces the rate of tunneling to form D + CO_2 products while increasing the lifetime of DOCO* because of the higher density of states.

The OD + CO reaction was initiated in a slow-flow cell by photolyzing O_3 in a mixture of D_2, CO, and N_2 gases with 266-nm (32-mJ, 10-Hz) pulses from a frequency-quadrupled Nd:YAG laser, expanded to a profile of 44 mm × 7 mm and entering the cell perpendicular to the cavity axis. The initial concentration of O_3, $[O_3]_0$, was fixed at a starting concentration of 1×10^{15} molecules cm^{-3} and verified by direct ultraviolet (UV) absorption spectroscopy. The initial concentrations of CO, N_2, and D_2 were varied over the range 1 to 47 torr (0.13 to 6.3 kPa), whereas the O_3 concentration was restricted to 3 to 300 mTorr (4×10^{-4} to 4×10^{-2} kPa) to minimize secondary reactions. A complete description and tabulation of the experimental conditions is included in section 1 of the supplementary materials.

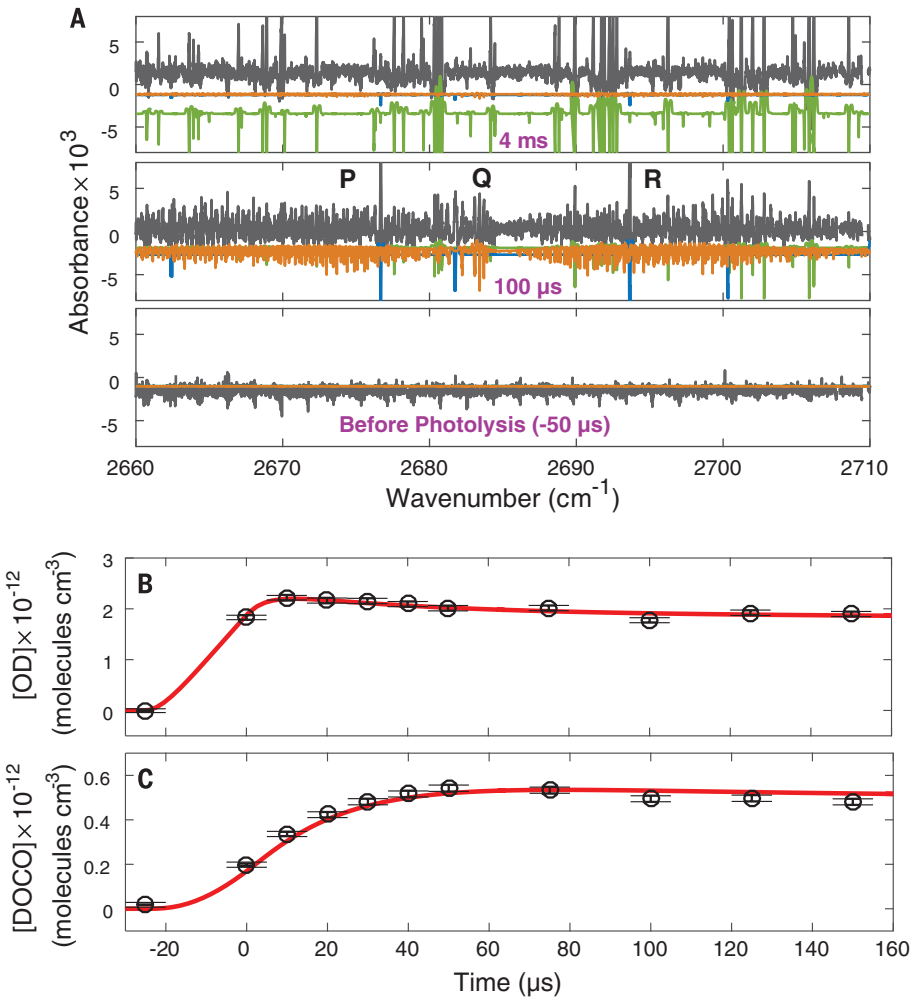

Fig. 2. Spectral acquisition and fitting. (**A**) Experimental spectra (black) were recorded with an integration time of 50 μs and offsets of −50 ("before photolysis"), 100, and 4000 μs from the photolysis pulse. These spectra were then fitted to the known line positions of OD (blue), D_2O (green), and *trans*-DOCO (orange) to determine their temporal concentration profiles. The P, Q, and R branches of *trans*-DOCO are indicated above the 100-μs experimental trace. (**B**) An analytical functional form for [OD](t) was obtained by fitting the data (black circles) to a sum of boxcar-averaged exponential functions (red line). At each time, the data point represents ~300 averaged spectra, and the error bars are from statistical uncertainties in the spectral fit. (**C**) The bimolecular *trans*-DOCO rise rate was obtained by fitting the data (black circles) to Eq. 3 (red line). The data in (B) and (C) were obtained at a 10-μs camera integration time and precursor concentrations of [CO] = 5.9×10^{17}, [N_2] = 8.9×10^{17}, [D_2] = 7.4×10^{16}, and [O_3] = 1×10^{15} molecules cm^{-3}.

Each photolysis pulse dissociated 15% of the ozone (supplementary materials, section 1) to form O_2 + $O(^1D)$ at nearly unity quantum yield (*26*). The resulting $O(^1D)$ either reacts with D_2 to form OD + D or is quenched by background gases to $O(^3P)$ within 1 μs. $O(^1D)$ + D_2 is known to be highly exothermic and produces vibrationally excited OD(v = 0 to 4) with an inverted population peaking at v = 2 and 3 (*27*). Vibrationally excited OD was rapidly quenched or formed D atoms by collisions with CO (*28*, *29*). Formation of vibrational Feshbach resonances of DOCO* from collisions of OD(v > 0) with CO may be possible, but the lifetimes are on the order of picoseconds, as previously observed for the HOCO* case (*30*–*33*). Therefore, only vibrationally and rotationally thermalized OD(v = 0) is expected to form DOCO by the mechanism described in the inset of Fig. 1A. OD and DOCO reach a steady state after 100 μs through the cycling reactions depicted in Fig. 1B: D atoms produced from OD + CO → D + CO_2 react with O_3 to regenerate the depleted OD.

Absorption spectra covering a ~65 cm^{-1} bandwidth were recorded at a sequence of delays from the time t = 0 photolysis pulse, using a camera integration time of either 10 or 50 μs, depending on the sensitivity to *trans*-DOCO signals. The broad bandwidth of the comb covers 6 OD, ~200 D_2O, and ~150 *trans*-DOCO transitions. These spectra were normalized to a spectrum acquired directly preceding the photolysis pulse and were fitted to determine time-dependent concentrations. With this approach, we captured the time-dependent kinetics of *trans*-DOCO, OD, and D_2O from OD + CO within a spectral window of 2660 to 2710 cm^{-1}. Representative snapshots at three different delay times are shown in Fig. 2A. The OD and *trans*-DOCO data were compared to simulated spectra, generated with PGopher (*34*) by using measured molecular constants (*35*–*37*) and known or computed intensities. The simulated spectra are fitted to these experimental data at each time delay to map out the full time trace of the three observed species (Fig. 2, B and C), with error bars derived directly from the fit residual. Section 2 of the supplementary materials includes details of the data analysis.

We determined the effective bimolecular rate coefficient for the *trans*-DOCO channel, $k_{1a}([M], T)$, from simultaneous measurements of time-dependent *trans*-DOCO and OD. In the low-pressure regime studied here, the DOCO formation rate obeys a termolecular rate law, whereas the effective bimolecular coefficient for the D + CO_2 channel remains close to the zero-pressure value, $k_{1b}([M] = 0)$. We measured the dependence of the effective bimolecular rate constant on the concentrations of all of the major species present in the experiment (N_2, CO, D_2, and O_3).

We analyzed the early-time (t < 200 μs) rise of *trans*-DOCO to decouple the measurement of k_{1a} from secondary loss channels at longer

Downloaded from http://science.sciencemag.org/ on October 27, 2016

times. The expected time dependence of the DOCO concentration is given by

$$\frac{d[\mathrm{DOCO}]}{dt} = k_{1a}[\mathrm{CO}][\mathrm{OD}](t) - k_{\mathrm{loss}}[\mathrm{X}][\mathrm{DOCO}](t) \quad (2)$$

k_{loss} describes a general DOCO decay through a reaction with species X, and [OD](t) refers to the time-dependent concentration of OD in the ground vibrational state. The solution to Eq. 2 is a convolution of the DOCO loss term with [OD](t), given by the integral in Eq. 3 (u is a dummy variable). [CO] is in large excess and remains constant throughout the reaction.

$$[\mathrm{DOCO}](t) = k_{1a}[\mathrm{CO}]\int_0^t e^{-(k_{\mathrm{loss}}[\mathrm{X}])(t-u)}[\mathrm{OD}](u)du \quad (3)$$

The effective bimolecular rate coefficient k_{1a} can be reduced into two terms dependent on N_2 and CO concentrations

$$k_{1a} = k_{1a}^{(\mathrm{CO})}[\mathrm{CO}] + k_{1a}^{(\mathrm{N_2})}[\mathrm{N_2}] \quad (4)$$

where $k_{1a}^{(\mathrm{CO})}$ and $k_{1a}^{(\mathrm{N_2})}$ are the termolecular rate coefficients with a third-body dependence on CO and N_2, respectively.

By simultaneously fitting [DOCO](t) and [OD](t) as a function of [CO] and [N_2], we uniquely determined all of the k_{1a} termolecular coefficients. Figure 2B shows an early-time segment of our data at 10-μs camera integration for both [*trans*-DOCO](t) and [OD](t). To fit the nonlinear time dependence of [OD](t), we used derived analytical functions composed of the sum of boxcar-averaged exponential rise and fall functions (supplementary materials, section 3). Equation 3 gives the functional form for fitting [*trans*-DOCO](t), which includes the integrated [OD](t) over the fitted time window of −25 to 160 μs. The fitted parameters are k_{1a} and a *trans*-DOCO loss rate, $r_{\mathrm{loss,exp}}$ ($\equiv k_{\mathrm{loss}}[\mathrm{X}]$).

For our first set of data, we varied the CO concentration. For each set of conditions, we acquired data at both 10- and 50-μs camera integration times. By plotting k_{1a} versus [CO] at 10 and 50 μs, we did not observe any systematic dependence on camera integration time. Moreover, we observed a clear linear dependence (with reduced chi-squared, $\chi^2_{\mathrm{red}} = 0.86$), indicating a strong termolecular dependence of k_{1a} on CO, or $k_{1a}{}^{(\mathrm{CO})}$ (Fig. 3A). The offset in the linear fit comes from the N_2 termolecular dependence of k_{1a}, or $k_{1a}^{(\mathrm{N_2})}$. We then varied N_2 concentration and observed a similar linear dependence of k_{1a} from Eq. 4. A 50-μs camera integration time was used for this second data set because of the lower *trans*-DOCO signals at higher N_2 concentrations. The results are shown in Fig. 3B. Because the offset terms from the linear fit to the CO data and the linear fit to the N_2 plot both correspond to $k_{1a}^{(\mathrm{N_2})}$, we performed a multidimensional linear regression to Eq. 4 to determine $k_{1a}^{(\mathrm{CO})}$, $k_{1a}^{(\mathrm{N_2})}$, and r_{loss} simultaneously. Because $r_{\mathrm{loss,exp}}$ describes *trans*-DOCO loss, it is expected to be invariant to [CO] and [N_2]. Therefore, $r_{\mathrm{loss,exp}}$ serves as a shared, fitted constant in the global fit across the CO and N_2 data sets. From the fits shown in red in Fig. 3, A and B, we obtained $k_{1a}^{(\mathrm{N_2})} = (9.1 \pm 3.6) \times 10^{-33}$ cm^6 molecules^{-2} s^{-1}, $k_{1a}^{(\mathrm{CO})} = (2.0 \pm 0.8) \times 10^{-32}$ cm^6 molecules^{-2} s^{-1}, and $r_{\mathrm{loss,exp}} = (4.0 \pm 0.4) \times 10^4$ s^{-1}. The statistical and systematic errors in these parameters are given in table S4.

To verify the reaction kinetics, we constructed a rate equation model of the OD + CO chemistry, which included the decay channels from secondary chemistry, to fit the *trans*-DOCO and OD time traces up to 1 ms (supplementary materials, section 4). We fit one overall scaling factor for both OD and *trans*-DOCO, which accounts for uncertainties in (i) the optical path length and (ii) photolysis yield and subsequent OD* quenching reactions that establish the initial steady-state concentration of OD. We also fit an additional *trans*-DOCO loss, $r_{\mathrm{loss,model}}$, to correctly capture the *trans*-DOCO concentration at t > 100 μs.

The *trans*-DOCO + O_3 → OD + CO_2 + O_2 rate coefficient (*9*) ($k_{\mathrm{O_3+DOCO}} \approx 4 \times 10^{-11}$ cm^3 molecules^{-1} s^{-1}) and the OD + CO termolecular rate coefficients from our experimentally measured values were fixed in the model. Representative fits for two different conditions based on the same rate equation model are shown in Fig. 4, A and B. We found good fits ($\chi^2_{\mathrm{red}} = 0.71$) with a single, consistent set of parameters over a wide range of CO, N_2, and O_3 concentrations, giving $r_{\mathrm{loss,model}} = (4.7 \pm 0.7) \times 10^3$ s^{-1} for all conditions (fig. S13A). The sum of loss contributions from $k_{\mathrm{O_3+DOCO}}[\mathrm{O_3}]$ and an additional loss from $r_{\mathrm{loss,model}}$ gives a total loss of ~4.5×10^4 s^{-1}, consistent with our measured $r_{\mathrm{loss,exp}}$. One possibility for $r_{\mathrm{loss,model}}$ is a second product branching channel of *trans*-DOCO + O_3 to produce DO_2 + CO_2 + O. The slight discrepancy of the *trans*-DOCO data with the rate equation model in Fig. 4B is possibly due to the inadequately constrained loss processes at long delay times.

Sources of systematic uncertainty have been carefully evaluated. First, we considered the impact of vibrationally hot OD at early times. We constrained the population of vibrationally excited OD in our system by directly observing several hot band transitions from OD(v = 1) (fig. S7). We observed that CO is an efficient quencher of OD vibration, with a measured OD(v = 1) lifetime (fig. S8) that is consistent with the OD(v = 1) + CO quenching rate reported by Brunning *et al.* (*17*) and Kohno *et al.* (*29*). These measurements reveal that the lifetime is well below the minimum integration time of 10 μs and that [OD(v = 1)] is less than 10% of [OD(v = 0)] in this time window. Given that OD(v = 1) is expected to produce stabilized *trans*-DOCO less efficiently than OD(v = 0), the systematic effect caused by the vibrationally hot OD is estimated to be <10%, which has been included in our total error budget (table S4).

Another systematic uncertainty arises from the finite camera integration time, which is large relative to (50 μs) or comparable to (10 μs) the early *trans*-DOCO rise time. The recovered k_{1a} values from the two integration times are consistent with each other to within 21%, which we have included as a systematic uncertainty in our measurement (fig. S6).

A third source of systematic uncertainty comes from any factors that would cause deviations from Eq. 2; therefore, we investigated the dependence of k_{1a} on D_2 and O_3 concentrations. Additional experiments were conducted in the same manner as the CO and N_2 experiments, but varying [O_3] (1×10^{14} to 4×10^{15} molecules cm^{-3}) and [D_2] (7×10^{16} to 1×10^{18} molecules cm^{-3}). Under our experimental conditions and using a 50-μs camera integration window, we observed a weak dependence of k_{1a} on [O_3]

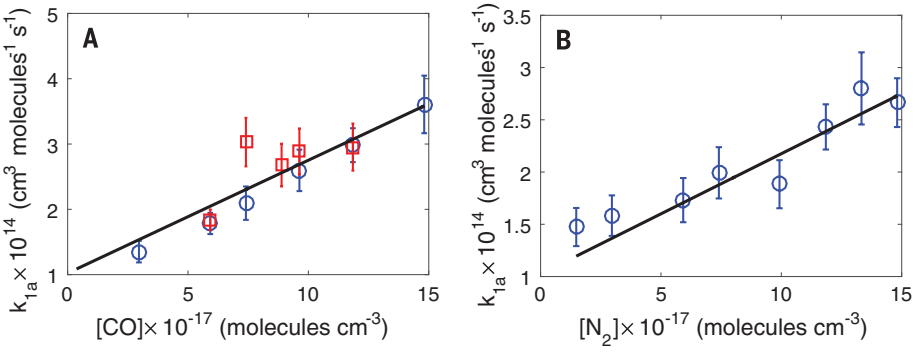

Fig. 3. Determination of the termolecular *trans*-DOCO formation rate. The bimolecular *trans*-DOCO formation rate coefficient, k_{1a}, is plotted as a function of [CO] and [N_2] to determine the termolecular rate coefficients $k_{1a}^{(\mathrm{CO})}$ and $k_{1a}^{(\mathrm{N_2})}$. Each point represents one of 26 experimental conditions tabulated in table S1. In both panels, the error bars represent uncertainties from fits to Eqs. 2 to 4 and the measured densities of the gases. (**A**) k_{1a} is plotted as a function of [CO] while [N_2] = 8.9×10^{17} molecules cm^{-3} is held constant. (**B**) k_{1a} is plotted as a function of [N_2] while [CO] = 5.6×10^{17} molecules cm^{-3} is held constant. In both plots, D_2 and O_3 concentrations are fixed at 7.4×10^{16} and 1×10^{15} molecules cm^{-3}, respectively. Blue and red data points indicate 50- and 10-μs camera integration times, respectively. The data in (A) and (B) are simultaneously fitted to Eq. 4. The black lines in (A) and (B) are obtained from weighted linear fits ($\chi^2_{\mathrm{red}} = 0.86$). The y offsets in the data arise from the nonzero concentrations of N_2 and CO in (A) and (B), respectively.

Downloaded from http://science.sciencemag.org/ on October 27, 2016

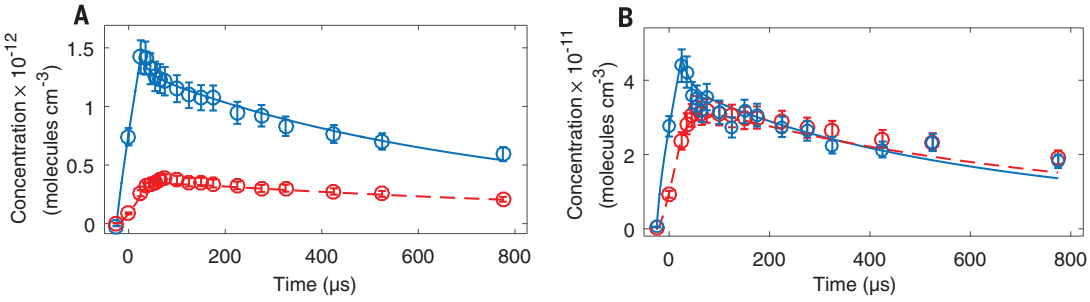

Fig. 4. Rate equation model fitting. The OD (blue circles) and *trans*-DOCO (red circles) traces are weighted fits to the model (solid and dashed lines for OD and *trans*-DOCO, respectively) described in the supplementary materials. The integration time was 50 μs. The error bars are from uncertainties in the spectral fit, in the same manner as for Fig. 2B. The input k_{1a} values for both CO and N_2 were from the early-time *trans*-DOCO rise analysis and were fixed in the fit. The floated parameters included a single scaling factor for the OD and *trans*-DOCO intensities and an extra DOCO loss channel. (**A**) [CO] = 5.9×10^{17} molecules cm^{-3}. (**B**) [CO] = 1.2×10^{18} molecules cm^{-3}. For both data sets, [N_2] = 8.9×10^{17}, [D_2] = 7.4×10^{16}, and [O_3] = 1×10^{15} molecules cm^{-3} were fixed.

(fig. S11) and no statistically significant variation with [D_2] (fig. S10). The O_3 dependence was measured at a CO concentration of 1.5×10^{17} molecules cm^{-3}. From analysis of the early-time *trans*-DOCO rise as a function of [O_3] and [D_2], we determined that O_3 and D_2 contribute an additional 11 and 8% statistical uncertainty, respectively, to our total budget (table S4).

We found that CO is ~100% more effective as a collision partner than N_2 in promoting the termolecular association of *trans*-DOCO. This result was missed in previous studies, which minimized the CO concentration (<4×10^{16} molecules cm^{-3}) to avoid biasing a pseudo–first order kinetics measurement (*12*, *38*). One might naïvely expect CO to be similar to N_2 as a third body; the significant difference observed here could be due to (i) near-resonant energy transfer between CO and the CO mode in DOCO, (ii) a stronger interaction potential between CO and DOCO*, or (iii) an influence of more efficient CO on OD(v) quenching for which we have not correctly accounted.

In the low-pressure regime, our measurements of the association rate coefficient, k_{1a}, can be compared to the pressure dependence of the overall rate of OD + CO, k_1, measured in previous experiments in N_2. Most of the pressure dependence of k_1 comes from k_{1a}, because k_{1b} is expected to change only slightly in this range. The termolecular (linear) components of the reported k_1 values from earlier studies by Paraskevopoulos *et al.* (*14*) and Golden *et al.* (*11*) fall within 1σ of our measured $k_{1a}^{(N_2)}$, which may suggest a k_{1a} contribution to the previously reported k_1. Apparent curvature in the pressure dependence observed elsewhere suggests that k_{1a} may already be in the fall-off regime. To estimate the *trans*-DOCO branching yield {percent yield ≈ $k_{1a}/[k_{1a} + k_1(\text{total pressure } p = 0 \text{ torr})]$}, we took the average value of k_1 from Paraskevopoulos *et al.* (*14*), Golden *et al.* (*11*), and Westenberg *et al.* (*39*). Even at low total pressures (75 torr of N_2), our results show that OD + CO produces a *trans*-DOCO yield of nearly 28 ± 11%.

Optical frequency comb spectroscopy allows broadband, time-resolved absorption detection of radicals with exceptional sensitivity and high spectral resolution. Our results demonstrate the capabilities of time-resolved cavity-enhanced direct frequency comb spectroscopy to elucidate chemical mechanisms through the quantitative detection of intermediates and primary products in real time. Our quantification of the termolecular dependence reveals additional factors that affect the product branching of the OH + CO reaction, which must be included in future atmospheric and combustion model predictions. For example, sensitivity analyses by Boxe *et al.* (*40*) have shown that, depending on the branching ratio, HOCO could contribute 25 to 70% of the total CO_2 concentration in the Martian atmosphere. Our experiment can be readily extended to detect other primary products (DO_2 or CO_2), as well as to study the OH/HOCO system. Furthermore, dynamics and nonthermal processes such as chemical activation, energy transfer, and rovibrational state-specific kinetics can be studied. With the bandwidth of optical frequency comb sources spanning an octave or more, the potential of this approach has not yet been fully realized. The technologies of frequency comb sources, detection methods, and mirror coatings are developing rapidly and will allow for more expansive applications of this multiplexed technique to many other important chemistry problems.

REFERENCES AND NOTES

1. A. W. Jasper *et al.*, *Science* **346**, 1212–1215 (2014).
2. T. L. Nguyen, B. C. Xue, R. E. Weston Jr., J. R. Barker, J. F. Stanton, *J. Phys. Chem. Lett.* **3**, 1549–1553 (2012).
3. J. S. Francisco, J. T. Muckerman, H. G. Yu, *Acc. Chem. Res.* **43**, 1519–1526 (2010).
4. C. J. Johnson, R. Otto, R. E. Continetti, *Phys. Chem. Chem. Phys.* **16**, 19091–19105 (2014).
5. J. Lelieveld *et al.*, *Nature* **452**, 737–740 (2008).
6. R. L. Mauldin 3rd *et al.*, *Nature* **488**, 193–196 (2012).
7. I. W. M. Smith, R. Zellner, *J. Chem. Soc., Faraday Trans. II* **69**, 1617–1627 (1973).
8. J. Troe, *J. Chem. Phys.* **75**, 226–237 (1981).
9. D. Fulle, H. F. Hamann, H. Hippler, J. Troe, *J. Chem. Phys.* **105**, 983–1000 (1996).
10. C. W. Larson, P. H. Stewart, D. M. Golden, *Int. J. Chem. Kinet.* **20**, 27–40 (1988).
11. D. M. Golden *et al.*, *J. Phys. Chem. A* **102**, 8598–8606 (1998).
12. D. C. McCabe, T. Gierczak, R. K. Talukdar, A. R. Ravishankara, *Geophys. Res. Lett.* **28**, 3135–3138 (2001).
13. G. Paraskevopoulos, R. S. Irwin, *J. Chem. Phys.* **80**, 259–266 (1984).
14. G. Paraskevopoulos, R. S. Irwin, *Chem. Phys. Lett.* **93**, 138–143 (1982).
15. M. J. Frost, P. Sharkey, I. W. M. Smith, *Faraday Discuss.* **91**, 305–317 (1991).
16. M. J. Frost, P. Sharkey, I. W. M. Smith, *J. Phys. Chem.* **97**, 12254–12259 (1993).
17. J. Brunning, D. W. Derbyshire, I. W. M. Smith, M. D. Williams, *J. Chem. Soc., Faraday Trans. II* **84**, 105–119 (1988).
18. R. E. Weston Jr., T. L. Nguyen, J. F. Stanton, J. R. Barker, *J. Phys. Chem. A* **117**, 821–835 (2013).
19. W. C. Chen, R. A. Marcus, *J. Chem. Phys.* **123**, 094307 (2005).
20. C. H. Chang, G. T. Buckingham, D. J. Nesbitt, *J. Phys. Chem. A* **117**, 13255–13264 (2013).
21. T. Oyama, W. Funato, Y. Sumiyoshi, Y. Endo, *J. Chem. Phys.* **134**, 174303 (2011).
22. M. C. McCarthy *et al.*, *J. Chem. Phys.* **144**, 124304 (2016).
23. A. J. Fleisher *et al.*, *J. Phys. Chem. Lett.* **5**, 2241–2246 (2014).
24. F. Adler *et al.*, *Opt. Lett.* **34**, 1330–1332 (2009).
25. G. D. Cole *et al.*, *Optica* **3**, 647–656 (2016).
26. J. C. Brock, R. T. Watson, *Chem. Phys. Lett.* **71**, 371–375 (1980).
27. J. E. Butler, R. G. Macdonald, D. J. Donaldson, J. J. Sloan, *Chem. Phys. Lett.* **95**, 183–188 (1983).
28. M. Brouard, D. W. Hughes, K. S. Kalogerakis, J. P. Simons, *J. Chem. Phys.* **112**, 4557–4571 (2000).
29. N. Kohno, M. Izumi, H. Kohguchi, K. Yamasaki, *J. Phys. Chem. A* **115**, 4867–4873 (2011).
30. N. F. Scherer, L. R. Khundkar, R. B. Bernstein, A. H. Zewail, *J. Chem. Phys.* **87**, 1451–1453 (1987).
31. S. I. Ionov, G. A. Brucker, C. Jaques, L. Valachovic, C. Wittig, *J. Chem. Phys.* **99**, 6553–6561 (1993).
32. D. C. Clary, G. C. Schatz, *J. Chem. Phys.* **99**, 4578–4589 (1993).
33. M. I. Hernández, D. C. Clary, *J. Chem. Phys.* **101**, 2779–2784 (1994).
34. C. Western, *J. Quant. Spectro. Rad. Transfer* 10.1016/j.jqsrt.2016.04.010 (2016).
35. J. T. Petty, C. B. Moore, *J. Chem. Phys.* **99**, 47–55 (1993).
36. M. C. Abrams, S. P. Davis, M. L. P. Rao, R. Engleman, *J. Mol. Spectrosc.* **165**, 57–74 (1994).
37. R. A. Toth, *J. Mol. Spectrosc.* **195**, 98–122 (1999).
38. Y. Liu, S. P. Sander, *J. Phys. Chem. A* **119**, 10060–10066 (2015).
39. A. A. Westenberg, W. E. Wilson, *J. Chem. Phys.* **45**, 338–342 (1966).
40. C. S. Boxe *et al.*, *Icarus* **242**, 97–104 (2014).

ACKNOWLEDGMENTS

Additional data supporting the conclusions are available in supplementary materials. We thank K. Sung of the NASA Jet Propulsion Laboratory (JPL) for providing a list of D_2O mid-IR line positions and intensities measured by R. A. Toth of JPL. We acknowledge financial support from the Air Force Office of Scientific Research, the Defense Advanced Research Projects Agency (DARPA) Spectral Combs from UV to THz (SCOUT) program, the National Institute of Standards and Technology, NSF, and DARPA (grants FAA-9550-14-C-0030 and W31P4Q-16-C-0001). M.O. is supported by NSF grant CHE-1413712. T.Q.B. and B.S. are supported by the National Research Council Research Associate Fellowship, P.B.C. is supported by the NSF Graduate Research Fellowship Program, and O.H.H. is partially supported through a Humboldt Fellowship. P.H., D.F., and C.D. are employees of a startup company (Crystalline Mirror Solutions), cofounded by G.D.C. and M.A., and coinventors on a submitted patent focusing on the crystalline mirror technology applied in this Report.

SUPPLEMENTARY MATERIALS

www.sciencemag.org/content/354/6311/444/suppl/DC1
Materials and Methods
Figs. S1 to S13
Tables S1 to S4
References (*41*–*62*)

20 May 2016; resubmitted 24 August 2016
Accepted 28 September 2016
10.1126/science.aag1862

Downloaded from http://science.sciencemag.org/ on October 27, 2016